Double field of view digital sideband holography as an optimized method to measure velocity fields in a large fluid volume

Ana Mª López Torres [a], Julia Lobera Salazar [a], Nieves Andrés Gimeno [a], Adrián Subías Martín [a], Eva Mª Roche Seruendo [a], Francisco José Torcal Milla [a], Mª Pilar Arroyo de Grandes [a], Jordi Pallarés Curto [b], Virginia Palero Díaz [a,*]

[a] *Instituto de Investigación en Ingeniería de Aragón (I3A), Universidad de Zaragoza, Zaragoza, Spain*
[b] *Departamento de Ingeniería Mecánica, Universitat Rovira i Virgili, Campus Sescelades, Tarragona, Spain*

ARTICLE INFO

ABSTRACT

Digital in-line holography is a technique that allows the measurement of the three velocity components of a three dimensional fluid flow. The application of digital in-line holography in fluid velocimetry is mainly limited by three factors: the sensor size that limits the transversal area that can be recorded, the low optical aperture that reduces the spatial resolution along the optical axis and introduces aliasing, and the noise coming from the twin image that hinders the particle position and velocity measurements. These factors do not affect in the same way when characterizing the movement of the fluid, and require different solutions.

In this work we are going to show how to overcome those limitations. We applied digital sideband holography for the measurement of the particle position and velocity in a fluid volume with a cross-section twice the area allowed by the camera sensor, with magnification $M = 1$, and a very large the dimension along the optical axis. Digital sideband holography configuration, that keeps the simplicity of the classical in-line holographic set-up, consists of a camera, a lens and a frequency filter. This frequency filter is the key element that allows us to measure in such a large volume while maintaining spatial resolution, as well as accuracy: not only removes the twin image but also prevents the recording of unwanted frequencies that causes aliasing. We have found that the Signal to Noise Ratio depends mainly on the noise introduced by the twin image, the aliasing and the particle concentration rather than on parameters such as field of view, depth of field or the intensity of the particles.

This technique is applied for the quantitative characterization of the three-dimensional flow in a lid-driven squared-sectioned cuvette. The introduction of a prism in the optical set-up allowed us to double the field of view. This is achieved by illuminating two volumes of the cuvette ($22 \times 22 \times 100$ mm^3, each) with the same beam that crosses the fluid twice before reaching the camera sensor. These two fluid volumes are analyzed independently while keeping the same spatial resolution in the axial component along the whole volume than the expected for a shorter one. The experimental 3D data show a very good agreement with numerical 3D simulation, which proves the very good performance of our method.

1. Introduction

Digital holography [1–3] is a measurement technique that is being applied widely in many scientific and industrial fields. Digital holography is based on the recording in a digital sensor (CCD or CMOS camera) of the interference of the light scattered by an illuminated object with a reference beam. The mathematical reconstruction of the hologram provides information of the amplitude and the phase of the object wave, which allows the recovering of many object features. As an example,

when it is applied to characterize fluid flows using the movement of tracer particles, it allows the accurate measurement of the 3D particle position, velocity and particle size [4–12].

In digital in-line holography (DIH), a translucent object is usually illuminated with a collimated beam. The light scattered by the object forms the so-called object beam and the unscattered light, forms the reference beam. This configuration presents several disadvantages. One is the well-known twin image problem [13–15]: the object virtual and real images are not fully separated when the hologram is reconstructed,

---

which adds noise to the reconstruction and prevents large particle concentration in the fluid. Another important drawback is the low system aperture, due to the sensor pixel size. Thus, the reconstructed particle image length along the observation direction is several times bigger than the real size. As a consequence, the accuracy in determining the position of the particle along the optical axis and the spatial resolution decrease. This circumstance is especially limiting for the regions furthest away from the sensor, where the defocusing and seeding density does not allow recording the particles clearly and completely. Finally, the flow cross-sectional dimension that can be recorded is limited by the size of the camera sensor, typically a few square centimeters. Despite these drawbacks, digital in-line holography is a powerful technique for measuring the three velocity components (3C) in a volume (3D) [16–20], and to obtain the particle size distribution [21].

The objective of this work is to measure the position and velocity of a large number of particles in a very large fluid volume while maintaining a high spatial resolution, as well as accuracy. In particular, we studied the confined, stationary flow generated in a squared-sectioned glass cuvette ($100 \times 100 \times 100 \text{mm}^3$) which top wall can rotate.

Our first challenge was to increase the recorded object cross-section, i.e. the field of view. This can be achieved by reducing the magnification (M). However, if M is much less than 1, the spatial resolution decreases significantly, implying losing information about small spatial structures. There are other practical drawbacks associated with illuminating a large cross-sectional area in a flow, such as the requirement for a collimating lens with a large enough diameter to ensure that the fluid is being evenly illuminated, or the need for the optical recording system to have a large enough numerical aperture.

Here, we doubled the field of view that can be recorded by the sensor at a magnification M≈1, illuminating two sections of the cuvette volume ($22 \times 22 \times 100 \text{mm}^3$ each) with the same beam that crosses the fluid twice before reaching the camera sensor (Fig. 2). The illuminating beam enters the cuvette by the wall nearer to the camera and travels to the opposite wall, where it is reflected with a rectangular prism. This second path, parallel to the first one, travels toward the camera sensor. As the illuminating beam travels through the fluid, the prism and the cuvette walls, the total path along the optical axis increases making the total recorded volume $22 \times 22 \times 368.3 \text{mm}^3$. One of the most remarkable features is that the volume longest dimension is parallel to the optical axis.

The next challenge was to measure the particle position and velocity with a high spatial resolution and accuracy in the whole volume. With this objective we used an experimental configuration which is often referred to as sideband holography [22–24]. The optical set-up is very simple, as it only requires a camera, a lens and a frequency filter to record the holograms. In the hologram recording only half of the object power spectrum is recorded, while the other half is blocked with a rectangular knife-edge aperture. Therefore, in the reconstruction, the real and virtual images of the aperture are completely separated and the twin image problem is solved. This rectangular aperture introduces an additional and essential advantage: it prevents the aliasing by cutting off the frequencies that are limited by the system aperture, i.e. by the sensor pixel size, and do not contribute to the signal. In fact, these two advantages of sideband holography allow the measurement in such a big volume. We have found that when it comes to accurately measuring the velocity field of a large set of particles, the Signal to Noise Ratio (SNR) depends mainly on the unwanted frequencies that are recorded in the hologram and on the particle concentration rather than on parameters such as field of view, depth of field or the intensity of the particles.

Hologram reconstruction and analysis has been carried out adapting a method outlined in [20] to the present experiments. The strength of this method lies in a fully automatic, adaptive process that provides the three components of the particle position with very high accuracy. Particle velocity is obtained with a method called Adaptive Cross Correlation with Tracking From Beginning (ACCTFB), which combines the 3D cross-correlation of the reconstructed intensity for measuring the

transversal velocity coordinates (Vx,Vy) and the 3D cross-correlation of the reconstructed object complex amplitude for measuring Vz. The good performance of this method is increased by the use of spherical glass particles that perform as point particles. Thus, when particles are located, their intensity is no longer a determining factor and they are selected by their position in the volume. Besides, the sideband set-up increases its robustness in such a way that it allows maintaining the accuracy in volumes twice as large.

In the next sections we are going to introduce the theoretical base of the measurement technique. Next, we will describe the experimental set-up and the influence of different parameters as the defocus distance, axial dimension of the studied volume or particle concentration will be discussed. The experimental 3D data show a very good agreement with numerical 3D simulation, which proves the very good performance of our method.

2. Digital sideband holography

Digital sideband in-line holography has two features that are not present in "conventional" in-line holography: the lens and the aperture located in the lens focal plane.

The lens forms the image of the object in the camera sensor, where it interferes with the part of the illumination that forms the reference beam. Thus, the camera is recording a so-called image hologram of the particle field. At the same time, the power spectrum of the particle field is formed in the focal plane of the lens. Furthermore, we can find a bright spot in the center of the focal plane of the lens that corresponds to the collimated illumination beam. These two elements can be considered as the object and the reference beam source of a lensless Fourier hologram, respectively. By calculating the Fourier transform of the recorded intensity field, we find that the particle distribution power spectrum is duplicated, since the recorded interference pattern is a real function. Therefore, it is possible to select only half of the spectrum with an appropriated filter (while blocking the other half) without losing significant information [15]. In practice, the filter can be as simple as a piece of black cardboard sheet where a rectangular aperture has been cut out. However, this simple aperture is the key factor that allows us to study such a big volume as not only removes the twin image but it prevents the aliasing by cutting off the frequencies that do not contribute to the signal and only add noise.

When a hologram with the aperture in the lens focal plane is recorded (Fig. 1a), particle images appear as half-moons [23]. The Fourier transform of the hologram shows the real and virtual images of the recorded part of the power spectrum, that is, the part that passes through the aperture. These images are completely separated, as in a lensless Fourier hologram (Fig. 1b).

Let us explain the process in detail. We are going to use the angular spectrum method, [25] in which the complex amplitude of the object
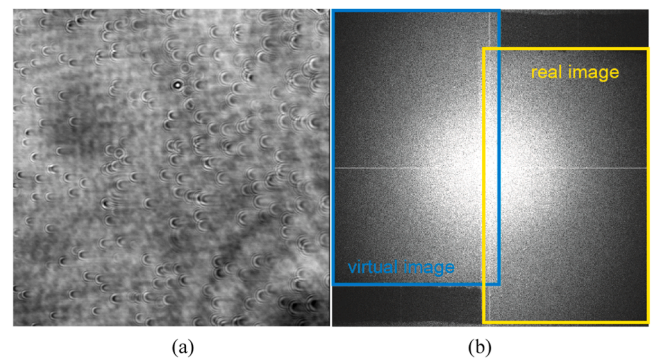

Fig. 1. a) Example of a sideband hologram of particles over a flat glass. b) Fourier transform of the hologram. The real (yellow) and virtual (blue) images of the aperture appear clearly separated, except for a small region in the center.

scattered field, $o(\overrightarrow{r})$, at a position given by $\overrightarrow{r} = (x, y, z)$, is given as a function of its spectral components, $O(\overrightarrow{k})$, as [26–28]:

$$o(\overrightarrow{r}) = \int_{-\infty}^{+\infty} O\left(\overrightarrow{k}\right) \exp\left(i\overrightarrow{k} \cdot \overrightarrow{r}\right) d\overrightarrow{k}, \tag{1}$$

where $\overrightarrow{k} = (k_x, k_y, k_z)$ is the wave vector. If we consider that the diffracted scattering is measured at the far field only the propagating plane-waves, with a wave number $|\overrightarrow{k}| = 2\pi/\lambda$, are recorded. This reduces the measured spectral components to a spherical surface in the k-space, which implies that $\overrightarrow{k}$ has only two independent variables, as $k_z = \sqrt{k^2 - (k_x^2 + k_y^2)}$. In such a case $O(\overrightarrow{k})$ becomes a two-dimensional matrix.

In the hologram recording, we modify the object power spectrum by introducing a frequency filter, $F(\overrightarrow{k})$, in the lens Fourier plane. This filter is a band pass filter, designed in such a way that it will select only the frequencies below the camera sensor resolution, while blocking half of the object power spectrum. According to the Nyquist criterion, the maximum frequency of the recorded interference pattern is $f_{max} = 1/(2d_{x,sensor})$, where $d_{x,sensor}$ is the sensor pixel size. Thus, the frequency filter, $F(\overrightarrow{k})$, can be described in the frequency domain as:

$$F\left(\overrightarrow{k}\right) = \begin{cases} 1 & \begin{cases} 0 \le k_x \le \pi/d_{x,sensor} \\ -\dfrac{\pi}{d_{y,sensor}} \le k_y \le \dfrac{\pi}{d_{y,sensor}} \end{cases}, \\ 0 \to elsewhere \end{cases} \tag{2}$$

being usually $d_{x,sensor} = d_{y,sensor}$. Thus, in the hologram plane, placed at $\overrightarrow{r}_0 = (x, y, 0)$, the two-dimensional complex amplitude of the object can be expressed as:

$$o_F\left(\overrightarrow{r}_0\right) = \int_{-\infty}^{+\infty} O\left(\overrightarrow{k}\right) F\left(\overrightarrow{k}\right) \exp\left(i\overrightarrow{k} \cdot \overrightarrow{r}_0\right) d\overrightarrow{k}. \tag{3}$$

In the hologram plane *(Fig. 1a)* we record the interference between a reference beam r (x,y) and o_F (x,y) as:

$$\begin{aligned} I(x, y) &= |r(x, y) + o_F(x, y)|^2 \\ &= |r(x, y)|^2 + |o_F(x, y)|^2 + o_F(x, y)^* r(x, y) + o_F(x, y) r(x, y)^*. \end{aligned} \tag{4}$$

In the spatial domain, these four terms are mixed, but they can be separated in the frequency domain by calculating the Fourier Transform of the recorded intensity (Fig. 1b). The two first terms of Eq. (4) will produce a continuous term that lies in the center. For a smooth reference, with an approximately constant intensity, the Fourier Transform is a delta function which is equivalent to a very bright central point. The second term is equivalent to the centered spectrum of the object. Meanwhile, the third and fourth terms will produce the real and virtual images of the filtered object. Let us study only these terms:

$$\Im\{I(x, y)\} \approx \Im\{o_F(x, y)^* r(x, y) + o_F(x, y) r(x, y)^*\}. \tag{5}$$

Equation 5 can also be written as:

$$\Im\{I(x, y)\} \approx O(k_x, k_y) F(k_x, k_y) + O^*(-k_x, -k_y) F^*(-k_x, -k_y). \tag{6}$$

The filter that is placed on the Fourier plane is a 2D rectangular function. Therefore, we can calculate its conjugate, with no effect on it. However, this rectangular function is evaluated at other frequencies. For this reason, $F(\overrightarrow{k})$ is written inverted with respect to the origin of coordinates. When selecting one of the reconstructed images, the Fourier transform is multiplied by a function which is approximately $F'(k_x, k_y) \approx F(k_x, k_y)$. This multiplication has no effect on the first term, but completely cancels the second term. In fact, $F'(k_x, k_y)$ is a bit more restrictive than $F(k_x, k_y)$, since $F(k_x, k_y)$ must allow the reference wave to pass through in order to interfere with the object wave. In the

reconstruction, however, we need to eliminate its contribution. Then if we multiply Eq. (6) by $F'(k_x, k_y)$:

$$F'\left(k_x, k_y\right) \Im\{I(x, y)\} = F'\left(k_x, k_y\right) O\left(k_x, k_y\right). \tag{7}$$

The inverse Fourier transform produces the filtered complex amplitude of the object.

$$\Im^{-1}\left\{F'\left(k_x, k_y\right) \Im\{I(x, y)\}\right\} = \Im^{-1}\left\{F'\left(k_x, k_y\right) O\left(k_x, k_y\right)\right\} = o_F(x, y). \tag{8}$$

As already mentioned, the filter can be a piece of black cardboard sheet where a rectangular aperture has been cut out. The operation described in Eq. (7) is precisely what allows us to select the real image of this aperture. The dimension of the aperture is calculated considering the Nyquist criterion. The area in the Fourier plane with "recordable" information will be a centered square region whose size Δ depends on f_{max} such that $\Delta = 2\lambda D f_{max}$, where λ is the wavelength and D the distance between the Fourier plane and the hologram sensor. When the image is formed on the sensor plane D=Mf', M being the magnification and f' the lens focal length, and Δ can be calculated as:

$$\Delta = \frac{\lambda f' M}{d_{x,sensor}} \tag{9}$$

With a $\Delta \times \Delta$ size square mask placed in the lens focal plane, a classical DIH will be obtained. In the reconstruction, the twin images will appear overlapped, but this mask will effectively eliminate aliasing. By using a rectangular mask a ($\Delta/2 \times \Delta$), both aliasing and the twin image problem will be solved. In the hologram reconstruction, the complex amplitude distribution of the object wave at any plane, $o_{1F}(x, y, z)$, can be calculated as:

$$\begin{aligned} o_{1F}(\overrightarrow{r}) &= \int_{-\infty}^{+\infty} O\left(\overrightarrow{k}\right) F\left(\overrightarrow{k}\right) H\left(\overrightarrow{k}\right) \exp\left(i\overrightarrow{k} \cdot \overrightarrow{r}\right) d\overrightarrow{k} \\ &= \int_{-\infty}^{+\infty} O_F\left(\overrightarrow{k}\right) H\left(\overrightarrow{k}\right) \exp\left(i\overrightarrow{k} \cdot \overrightarrow{r}\right) d\overrightarrow{k}. \end{aligned} \tag{10}$$

Where $H(\overrightarrow{k})$ is given by:

$$H\left(\overrightarrow{k}\right) = \frac{\exp\left(ik \cdot \left|\overrightarrow{r} - \overrightarrow{r}_o\right|\right)}{ik\left|\overrightarrow{r} - \overrightarrow{r}_o\right|}. \tag{11}$$

In practice, equation 10 is calculated by applying the convolution method [1,25], as the inverse Fourier transform of the product of the Fourier transform of the filtered object, $O_F(\overrightarrow{k})$, and the transfer function, $H(\overrightarrow{k})$, as:

$$o_{1F}(\overrightarrow{r}) = FT^{-1}\left\{O_F\left(\overrightarrow{k}\right) H\left(\overrightarrow{k}\right)\right\}. \tag{12}$$
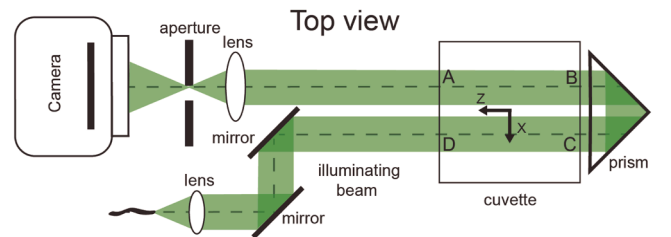

Fig. 2. Experimental set-up. The illumination beam enters the cuvette at D, leaves the fluid volume at C and, after crossing the prism, enters back into the cuvette at B. The beam leaves at A towards the lens that forms the image of the selected cuvette wall on the camera sensor. In the lens focal plane, the rectangular aperture selects half of the power spectrum and removes the high frequencies.

3. Experimental configuration and hologram recording considerations

In the following we will describe the experimental set-up (Fig. 2) designed to record a field of view twice the camera sensor size, while keeping M≈1. The squared-sectioned cuvette ($100 \times 100 \times 100mm^3$) made of optical glass (refractive index, n_{glass}=1.523), is illuminated with the same beam that crossed the fluid twice before reaching the camera sensor.

The illumination beam is carried by an optical fiber, collimated and redirected by means of a pair of mirrors, so that it enters the rectangular cuvette through the wall closest to the camera (cuvette wall D in Fig. 2). There, it travels to the cuvette opposite wall (C), where it is reflected back with a rectangular prism. In this second path, parallel to the first one, the beam travels towards the camera sensor from the plane B to A. In that way we can record two sections of the volume (H × W × L=22 × 22 × 100mm³ each), that are separated a certain distance in the X direction.

The liquid that fills the cuvette is a water-glycerin solution (60% v/v glycerin, refractive index, n_{fluid}=1.431). The flow has been seeded with glass spherical particles with diameter between 45 and 90 μm ($n_{particle}$=1.520). These transparent particles perform as point particles and their effective size is the sensor pixel size. The illuminating beam comes from a continuum laser which wavelength is λ=532nm. Working in fluid with refractive index n_{fluid}>1, makes the effective wavelength, or the wavelength in the fluid ($λ_f = λ/n_{fluid}$) smaller than the wavelength in air. In this case $λ_f$ =371.9nm.

As the illuminating beam travels through the prism and the cuvette, it crosses volumes with different refractive index which will increase the total optical path (OP). The OP in the liquid is 200 × 1.431=286.2mm. The cuvette walls have a width of 3.5mm (OP=5.33mm, each). The prism is 40 × 40mm, made of BK7 optical glass, n_{BK7}=1.519, and adds an OP=60.8mm. The total optical path added by these elements is 82.1mm, making a total path along the optical axis, in which we will find information about the particles, TOP=368.3mm. Therefore, the effective recorded volume is 22 × 22 × 368.3mm³. This volume is approximately centered in the X axis of the cuvette: AB goes from -21mm≤ X≤0mm and CD 9mm≤X≤ 30mm, and at Y=17mm over the cuvette bottom.

Holograms were recorded with a Photron SA2 camera (sensor size 2048 × 2048, 1000 fps) with a pixel size $d_{x,sensor}$=10μm and with a magnification, M=0.94. The lens is a MicroNikkor photographic objective (f'=105mm, minimum f#=2.8). As we reconstructed the holograms in the object domain, from now on we will use the effective pixel $d_x=d_{x,sensor}$/M=10.6μm and the fluid wavelength ($λ_f$). Therefore, the hologram reconstruction is done as if the whole volume has the same refractive index, and the void area has a corrected length.

The use of the lens allows us to choose the focusing plane and we have measured the velocity field focusing in the cuvette walls in three different positions (Fig. 3): in the wall nearer to the lens, marked with an A in Fig. 2 (in the following, we will call these experiments case A), in the wall B, where the beam enters the volume after crossing the prism (case B) and before the beam enters the prism (case C). Let's point out that we are using two coordinate systems, one for the hologram
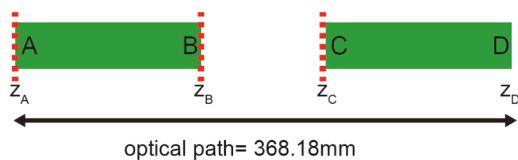

Fig. 3. Holograms are recorded focusing at different planes. The volume AB correspond to the X-negative zone of the cuvette (−21 mm< X< 0 mm), while CD contains information on the X-positive volume of the cuvette (9 mm < X < 30 mm).

reconstruction (in lowercase letter) and another for the representation of the fluid velocities (in capital letter).

The depth of field (the volume length along the optical axis that can be recorded) can impose a limit to our measured volume. Suppose we have a particle at a distance z from the plane of the hologram. In such a plane, the diffraction pattern of the particle will have a certain radius, R_{DP}, which is related with z and the angular aperture of the system, $σ_S$. In fact, R_{DP} is limited by the size of the hologram and must meet the following condition:

$$R_{DP} = σ_S z \leq \frac{N_x d_x}{2z}, \tag{13}$$

where N_x is the number of pixels in the x-direction. If the aperture is only limited by the pixel sensor size, as in our case, $σ_S=λ_f/2d_x$ and therefore:

$$z \leq \frac{N_x d_x^2}{λ_f}. \tag{14}$$

This result is similar to the one found in [29,30]. In our case, with N_x=2048, z_{max}=618.6mm, which means that even the image of the farther particles within our measured axial range will be fully recorded even for case A.

However, these calculations have been made for an isolated particle located in the center of the hologram and we are working in a densely seeded flow. Thus, we need to quantify the influence of other particles in the position and velocity measurement of a particle located at different distances from the hologram. Let us suppose again we have a particle **P** in z=z_p, with a radius R_p, and maximum scattered intensity i_o. We are going to consider two cases: the influence of particles located in z>z_p and particles located in z<z_p, where z=0 corresponds to the hologram plane.

Any particle is illuminated with a collimated beam, but **P** also receives the light diffracted by the particles in z>z_p. The effect of this non-uniform illumination on the particle detection is all or nothing: if **P** is not illuminated correctly, it will not be detected by our software or will be discarded in further analysis.

If, on the other hand, **P** is correctly illuminated, particles located in z<z_p, might block part of our particle's diffraction pattern: the reconstructed particle image will be affected, and it will be located with greater error than the non-affected particles. This fact can go unnoticed by the analysis and become only apparent when following the particle. When a series of holograms is recorded it could affect the image of the particle in the first exposure, or in the second exposure, even in both exposures differently. So the error could be in the position or in the velocity measurement. We can quantify this effect by calculating the intensity blocked per pixel, i_{bpp}, by the particles located at z<z_p. This blocked intensity depends on the particle concentration, the cross-section of the particle and the volume in front of **P**, i.e., the shadow density [31–33].

Particle concentration can be calculated as $ppp/(d_x^2(z_A - z_D))$, where ppp is particles per pixel, and (z_A-z_D) is the measured range, i.e., the distance between planes A and D. The intensity diffracted by **P** is distributed in an area that increases with z-z_p, A_{z-zp}. Therefore, the number of particles that can affect the particle image increases with A_{z-zp}. On the other hand, the fraction of the intensity blocked by any of these particles decreases with $πR_p^2/A_{z-zp}$. Thus, the blocked intensity can be considered roughly constant for any plane z between z_p and the first plane with particles z_A. Thus the total blocked intensity of the diffraction pattern can be estimated as:

$$i_{bpp}(z_p) = i_o \left(πR_p^2 \frac{ppp}{d_x^2(z_A - z_D)} \right)(z_p - z_A). \tag{15}$$

This result explains why particle images located further away from the hologram plane are more difficulty to recover. It also indicates that particle concentration will affect strongly the SNR, and that ppp is a key factor to measure in a large volume.

4. Hologram reconstruction, particle position and velocity measurement

We will distinguish two parts in the hologram analysis. The first one aims to determine the position of a set of particles in the volume and the second one is the particle tracking through a certain number of holograms. The analysis has been done by applying a procedure similar to the one described in [20] that has been adapted to the present case, where the sideband configuration has been used and where two big volumes with particles (inside the cuvette) that are separated by void areas (Fig. 3) are going to be analyzed. Our measurement includes regions A-B and C-D, but skips these void areas. It is important to note that only the areas belonging to the volume of the cuvette are being reconstructed, which implies that the information corresponding to each section is independently extracted by reconstructing the hologram at different axial ranges. This entire process is completely automatic and is not affected by the particle image shape.

In the reconstruction, the origin of the axial coordinate z is made to coincide with the hologram plane position. In particular, for case A, z=0 will be located in plane A and every reconstructed plane will have a z>0. Meanwhile, in cases B and C, z=0 will be located in B and C respectively, which implies that the particles in region AB are in z<0. Positive z planes (CD range) correspond to x-positive section, while negative z planes (AB range) belong to the x-negative volume. This introduces a certain complication, since it is necessary to change the software and the way in which the particles are searched for. The whole process is outlined in Figs. 4 and 5 for case B.

The fluid movement produces a shadowed area in the holograms. So, in an initial step, the holograms SNR must be enhanced. This structure changes during the recording time, which prevents us from using the whole series to compute the average hologram. A moving average is calculated for each hologram, taking the ten previous holograms and the next ten. The enhanced hologram is obtained after subtracting the moving average and normalizing its intensity.

Let us start with the first hologram. The reconstruction of the object complex amplitude starts (Fig. 4) by calculating the Fourier transform of the recorded intensity pattern and by selecting the real image of the aperture. Its inverse Fourier transform is calculated to obtain the complex amplitude distribution of the object wave. This is propagated at different z-planes (with a sampling interval d_z) inside the volume of the cuvette by using the convolution method.

The measurement of the position of the particles is based on the detection of intensity maxima in this reconstructed volume. The intensity $i_{1F}(x,y,z)$ is calculated from the object complex amplitude as:

$$i_{1F}(x, y, z) = |o_{1F}(x, y, z)|^2. \tag{16}$$

We will divide the volume in 3D interrogation windows (3DIW), which size will decrease in successive steps in order to increase the accuracy of the particle position measurement. In a first step, these 3DIW will extend over the whole length of the reconstructed volume, with dimensions $40 \times 40 \times (2L/d_z)$ pixel^3 (Fig. 5a). Pixels in the xy plane are defined by d_x and d_y. The longitudinal size of the reconstructed particle image R_z, helps to define the pixel size in z, i.e., the sampling interval d_z. R_z is directly related with the numerical aperture (NA) and with the effective wavelength λ_f. Here NA is mostly limited by the effective pixel size (d_x) in the x and y directions and R_z can be calculated as:

$$R_z = \frac{8d_x^2}{\lambda_f}. \tag{17}$$

In this case, R_z=2.42mm, is much bigger than the particle real size. Thus, considering R_z, we will take d_z=2mm and the first 3DIWs correspond to $0.424 \times 0.424 \times 200$mm^3. In order to optimize the volume sampling, the 3DIWs were overlapped a 50% in the xy plane, providing around 10000 maxima in the first hologram. Half of the detected maxima are spurious peaks or just oversampling due to the 3DIW overlapping and must be removed.

At this point we need to modify the procedure described in [20]. The recorded volume is so large that most particles will require using a 3DIW with a very big cross section, which will increase unreasonably the time and memory requirements of the algorithm. Besides, as we use point like particles, their intensity is no longer relevant. We will focus instead on particle position. The whole set of found maxima has to be divided in several sets according to its axial position. We have chosen to divide the fluid volume in two sections: AB and CD that will be analyzed sequentially. The appropriated number of sections in which the recorded volume could be divided depends on the specific experimental problem.

In the next step, we are going to compute again the object wave intensity around each found maximum to discriminate if it is a nice local maximum that can be associated to a particle and improve its location. We will start with the volume defined by AB, where we reconstruct the complex amplitude (o_{1F}(x, y, z_c), and then, the intensity from the central plane z_c=50mm instead of the hologram plane, using Eq. (10). The advantage of reconstructing the particles from the central plane of AB is that we can define new and smaller 3DIWs centered in the maximum found previously (Fig. 5b). We choose 500 particles on each section. These 3DIWs are calculated automatically, with an adaptive criterion based in the size of the diffraction pattern of a particle. The diffraction pattern cross section depends on the particle's position in z, being larger the further the particle is from the central plane. The 3DIWs cross section ($S_x \times S_y$) will be calculated with the size of the Airy disc of a circular aperture located at a distance, z_p, where S_x and S_y are defined as:

$$S_x \approx \frac{2.44\lambda}{d_x}\left(z_p - z_c\right), \ S_y = S_x. \tag{18}$$

The 3DIW final size is $(S_x/d_x) \times (S_y/d_y) \times 30$pixel^3 with d_z=0.2mm.

Particle position is measured from the information contained in these windows. However, the key to obtaining an accurate position is to use only the pixels that contribute the most to the particle's image and therefore define the particle (Fig. 5c). The pixels in the 3DIW are ordered from highest to lowest intensity and the cumulative sum is calculated in a vector, in such a way that its last element is the total cumulative sum. That accumulated sum vector is normalized by the total accumulated sum and the position of the threshold is found (in our case 0.64). Then, only the pixels whose intensity adds up the 64% of the total intensity are used to determine the particle position. The transversal coordinates (x, y) are given by the centroid of that final pixel distribution, while the particle z coordinate is calculated as the maximum of a quadratic polynomial fit. The particle is kept in the working set only if the new coordinates are close enough to the coarse maximum calculated previously, being the maximum shift allowed (Δx<0.025mm, Δy<0.025mm, Δz<3mm). Once the particles in AB are located, a second step is performed to locate the maxima (Fig. 5d) with the modified complex amplitude, o_{1F_M}, where the intensity of the particles located in AB has been removed. The 3DIW was again $40 \times 40 \times (2L/d_z)$ pixel^3, with the same pixel sizes as before. Then, particle localization, as described above, is carried out for the precise localization inside the CD volume (z = 60mm to 160mm) (Fig. 5e, f).

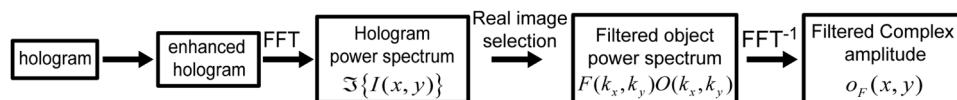After applying the algorithm restrictions to decide whether or not a

Fig. 4. Initial steps in reconstruction of the object complex amplitude.
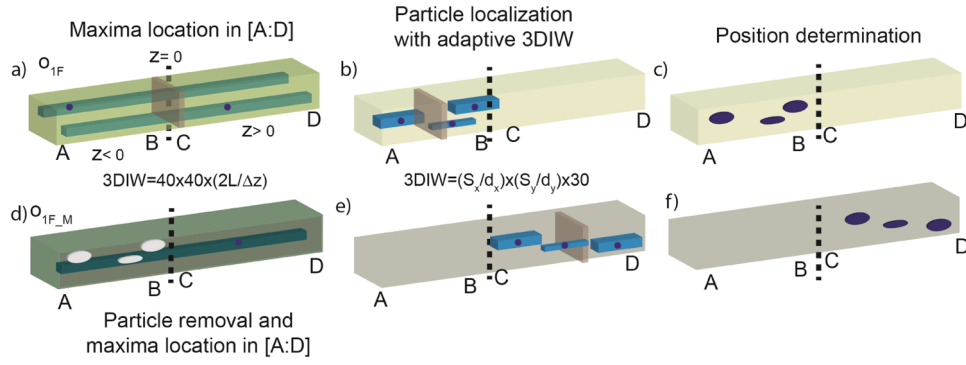
Fig. 5. Steps in the process of locating the initial set of particles: a) search for intensity maxima in the reconstructed volume; b) particle identification with adaptive 3DIW in the AB range; c) accurate coordinate measurement in the AB range; d) particles located in this first volume are removed and search for new intensity maxima; e) particle identification with adaptive 3DIW in the CD range; f) accurate coordinate measurement in the CD range.

location corresponds to a particle, an average of 250-300 particles per section is obtained. As it has been shown, the particles closest to the camera hinder the location of particles that are farther away. For this reason, the location and removal of particles must be done sequentially from the section AB (closest to the camera) to CD.

Once we have defined the particle set in the first hologram, these particles have to be tracked along a number of holograms in order to obtain the 3D velocity field. We applied a multi-pass, adaptive interrogation process called Adaptive Cross-Correlation Tracking From Beginning (ACCTFB). This method is based on the 3D cross-correlation of 3D interrogation windows, in a similar approach to the one used in Particle Image Velocimetry (PIV). The process is outlined in Fig. 6.

Particles in section AB have to be tracked first and removed from the hologram before tracking particles in CD. As before, we will propagate the object complex amplitude to the central plane of AB in the first and second holograms. The intensity is calculated and new 3DIWs ($40 \times 40 \times 15$pixel^3, $d_z=0.2$ mm), centered in the particle location obtained from the first hologram, are defined. A Gaussian filter is applied to the 3DIW, centered in the particle position in the first hologram, to highlight the particle against the background. Then, the 3D cross-correlation of the intensity distributions is calculated as:

$$C\left(\overrightarrow{r}_{3DIW}\right) = \left(i_{1F}\left(\overrightarrow{r}_{3DIW}\right)G\left(\overrightarrow{r}_{3DIW}\right)\right) \otimes i_{2F}\left(\overrightarrow{r}_{3DIW}\right). \qquad (19)$$

The correlation peak position will provide a first approach to the

particle displacement,$\Delta\overrightarrow{r}_2$. However, this first peak might be deformed due to the contribution of out-of-focus particles in the reconstructed volume. That contribution can be removed by applying another Gaussian filter to the 3DIW of the second hologram, centered in the position given by the correlation peak position. The intensity 3D cross-correlation is calculated again with an improved SNR.

$$C\left(\overrightarrow{r}_{3DIW}\right) = \left(i_{1F}\left(\overrightarrow{r}_{3DIW}\right)G\left(\overrightarrow{r}_{3DIW}\right)\right)$$
$$\otimes \left(i_{2F}\left(\overrightarrow{r}_{3DIW}\right)G\left(\overrightarrow{r}_{3DIW} - \Delta\overrightarrow{r}_2\right)\right). \qquad (20)$$

The new correlation peak is obtained by following the same method as the one described for defining a particle accurately. Only the pixels whose intensity adds up the 64% of the total intensity are considered to form the peak. The transversal particle displacement (Δx_2, Δy_2) and the particle velocity components (Vx$_2$=Δx_2/ΔT; Vy$_2$=Δy_2/ΔT) are calculated from the peak centroid. The particle position in the second hologram (x_2, y_2) is obtained by adding to the displacements the particle coordinates in the first hologram.

In order to calculate the displacement along the optical axis (Δz_2) a third cross-correlation is needed (Fig. 6b). However, we use the complex amplitude instead of the intensity as shown in [20]. The complex amplitude cross-correlation uses the whole information of the particle image, its amplitude and its phase, so it provides a sharper correlation
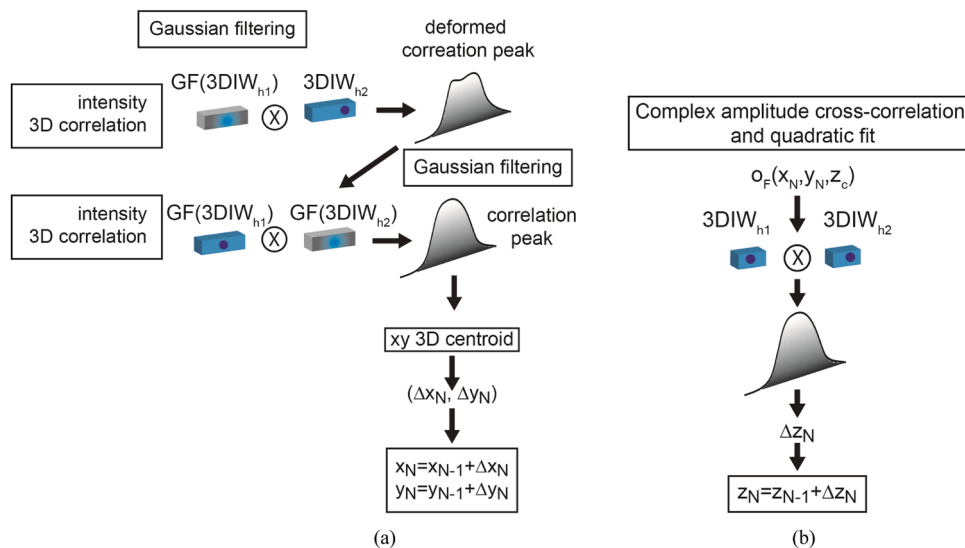

Fig. 6. Particle displacements calculation between the first and Nth holograms: a) first and second intensity cross-correlations; b) third complex amplitude cross-correlation with reduced interrogation window.

peak than the intensity cross-correlation [34,35]. The final size of the 3DIWs is reduced to the particle size ($8 \times 8 \times 15$ pixel^3; $d_z = 0.2$mm). In this way, the reconstructed particle images are not affected by the coherent noise coming from the out-of-focus particles that forced the use of the intensity correlation in the previous steps.

Once the three coordinates are found in the second hologram, the particle must be tracked along the hologram series to measure (Δx_N, Δy_N, Δz_N). The Tracking From Beginning relies in the calculation of the 3D cross-correlation between one 3DIW in the first hologram, centered in the particle, and a shifted 3DIW in the Nth hologram, but centered in the particle position obtained from the (N-1)th hologram. In that way, a small 3DIW size can be kept, as if the cross-correlation were performed between consecutive holograms, but avoiding the accumulative error that appears when consecutive recordings are used to follow a particle.

It is not possible to follow the particles along the whole recorded hologram series, since we are not observing the complete cuvette volume. New particles have to be included in the working set to replace those that are leaving the recorded volume. Restarting the analysis every fifty holograms has proved to be enough to have a complete flow description. This means that around 500 particles are followed along these 50 holograms. Then, a new working set of particles is found again and the whole procedure, including the Tracking from Beginning, is repeated.

5. Results

The analyzed flow was generated by the rotation of the cuvette's top wall. It is a disk (diameter 8cm) which is submerged 1cm within the fluid and rotates with an electronically controlled DC motor. The motor works with angular velocities (ω) from 5 to 25 rad/s. In our experiments, we selected $\omega = 17.06$ rad/s. The liquid that fills the cuvette is a water-glycerin solution (60% v/v glycerin). Its kinematic viscosity (ν) changes between 1.7×10^{-5} m^2/s and 2.5×10^{-5} m^2/s, within the range of room temperature of the experiments, and its density is $\rho \sim 1186$ kg/m^3. A photographic lens formed the volume image in the camera sensor with magnification M=0.94. The aperture in the lens focal plane was 5.25×2.625mm^2. Series of 1000 holograms, focusing at three different planes (A, B and C in Figs. 2 and 3) were recorded with a time interval between two consecutive holograms $\Delta T = 1$ms.

We designate as cases A, B and C the results obtained when we focus on plane A, B and C respectively. The focused plane in case A would be located in Z=0.05m (X<0), in case B in Z=-0.05m (X<0) and in case C, in Z=-0.05m (X>0). The region AB corresponds to the range of X<0, while CD corresponds to X>0. Fig. 7a shows an example of a hologram recorded with this set-up for case B. In Fig. 7b and 7c we show the reconstructed intensity in the central plane of volumes AB and CD respectively. In these images we can see focused and out-of-focus particles, as well as the noise that affects the hologram.
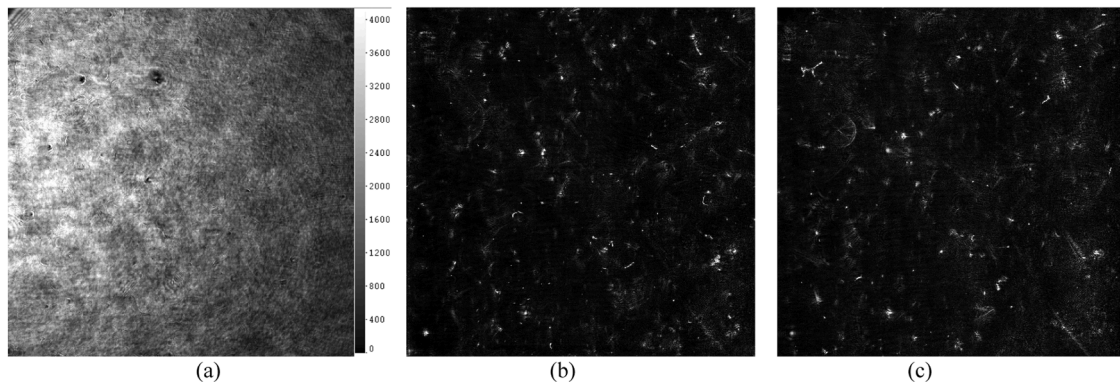
We have found that the 3D velocity fields are quite similar independently of the plane that has been focused in the recording. This can be seen in Fig. 8, where we are presenting the 3D velocity vector maps obtained for case A (Fig. 8a) and case C (Fig. 8b). Both maps are compared with the numerical simulation (Fig. 8c), corresponding at a viscosity of 2.5×10^{-5}m^2/s. Numerical simulations [36] have been performed with the commercial second-order, finite volume code ANSYS Fluent 2022. The flow is assumed to be incompressible and the fluid physical properties constant. For the conditions considered the flow is laminar and steady, and consequently the simulation has been carried out without any turbulence model. The computational model reproduces the flow configuration of the experiments with the same dimensions and the same rotation speed of the top cylindrical wall. Non-slip boundary conditions are applied on the solid walls and a zero shear stress boundary condition is imposed on the free surface. Simulations have been performed with meshes of 0.5M hexahedral elements, which are stretched near the static walls of the cavity and the rotating lid. A simulation with 0.3M elements gives very similar results.

The vector length is proportional to the velocity in each point and the color code corresponds to the velocity component. To have a better visualization, only one vector out of every 5 is represented. It is evident that Vx and Vy are very similar for cases A and C and show a very good agreement with the numerical simulation. The third velocity component, Vz, is quite noisy, although it is slightly better for case C. Nevertheless, it can be seen that the points with Vz>0 are in the zone predicted by the simulation and the same happens with the points with Vz<0.

Focusing in plane A, B or C does not have a significant influence in the measurement of the velocity field as we envisaged before from Eq. (14). However, according to Eq. (15), the noise introduced by the particles in a fluid with a very dense seeding, increases with the axial distance to the plane closer to the sensor (z_p-z_A). This noise reduces the SNR in the volume CD although is difficult to perceive it in the vector maps. By changing the velocity representation, signal loss becomes evident. Fig. 9 shows Vy versus Z for cases A and C. This velocity component should be axisymmetric but tends to zero in the region further away from the camera sensor.

Thus, the solution should be reducing the particle concentration. New experiments were performed with a reduced particle concentration. As the environmental conditions changed (humidity and temperature in the laboratory), the viscosity decreased to 1.7×10^{-5}m^2/s making the flow velocity increase. Fig. 10 shows Vy versus Z, in CD, for case B with the same ppp as in the measurements shown in Figs. 8 and 9, and with a reduced ppp. The symmetry in Vy with a reduced ppp is evident.

We can estimate the ppp from the recorded object intensity on the holograms. According to [31,32], assuming that the seeding particles are identical and are randomly distributed over the volume, the noise introduced into the hologram is the mean intensity of all particles. Thus,
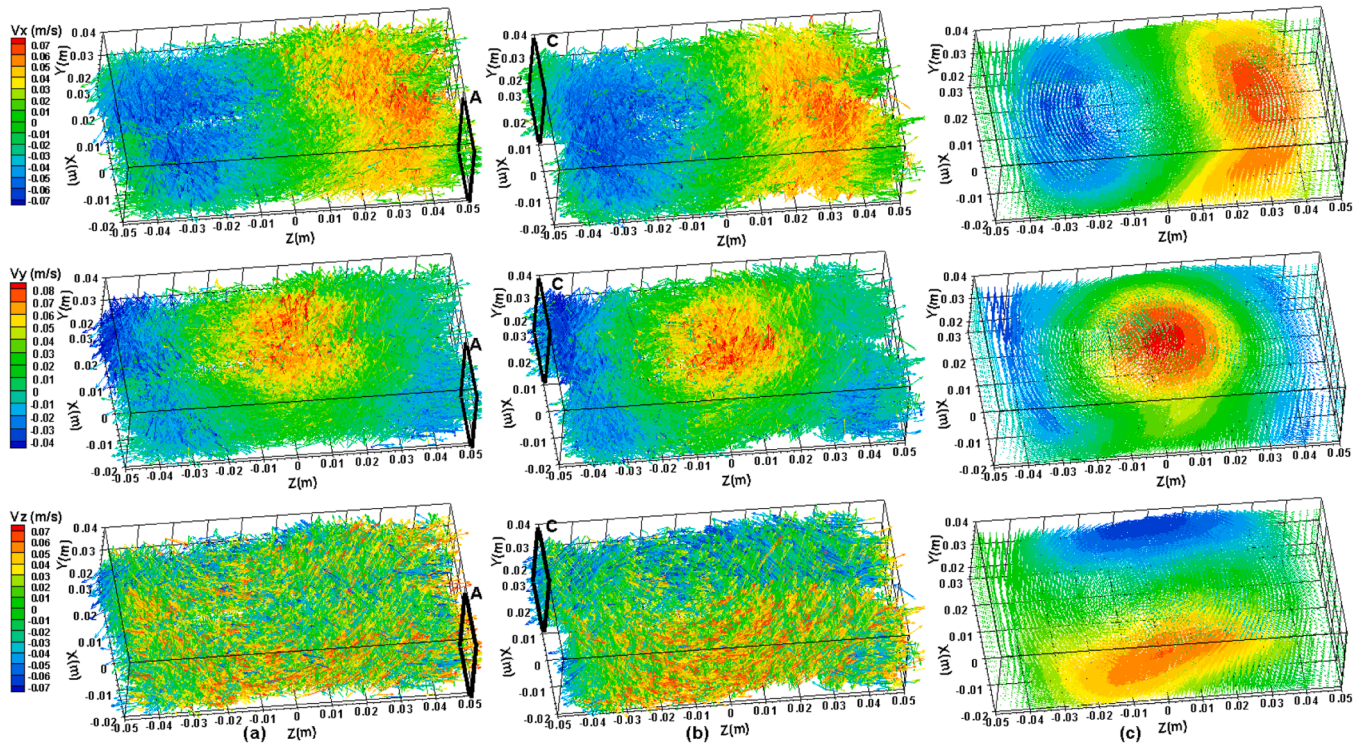

Fig. 7. a) Example of a hologram recorded for case B; b) reconstructed intensity in the central plane of volume AB; c) reconstructed intensity in the central plane of volume CD.

Fig. 8. Velocity vector maps obtained in the illuminated volume of the cuvette for a) case A; b) case C; c) numerical simulation.
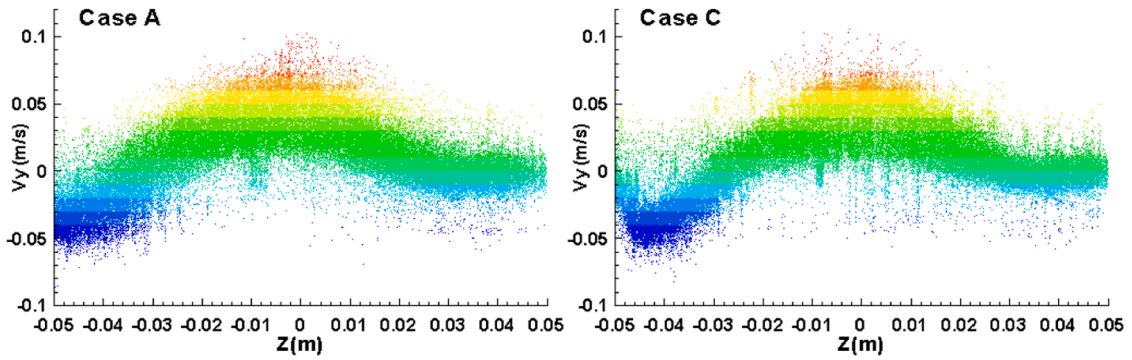

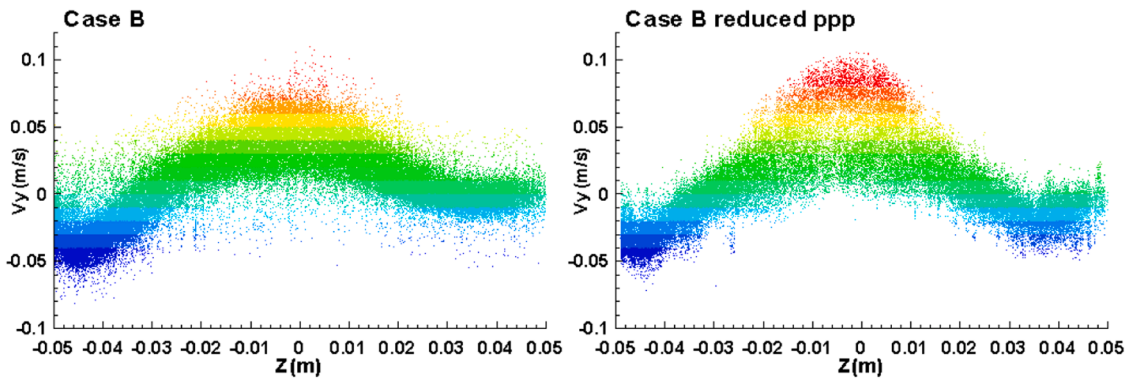**Fig. 9.** Vy versus Z, in volume CD, for cases A (left) and C (right).

Fig. 10. Vy versus Z, in volume CD, for case B with large (left) and reduced ppp (right).

the noise per pixel, i_{npp}, can be expressed as:

$$i_{npp} = ppp * i_o, \tag{21}$$

where i_o is the mean intensity scattered by any individual particle that can be computed as the mean intensity of the identified particles from a hologram with the procedure described in the previous section. The noise i_{npp} can be also computed from any hologram, after removing the background and the twin image, as the standard deviation of the resultant intensity. Thus, the SNR can be calculated as $SNR = i_o / i_{npp} = ppp^{-1}$, which gives a SNR=4.3 and ppp=0.23 for the experiments shown in Figs. 8 and 9, and SNR=16.5, ppp=0.06, for the data shown in Fig. 10.

A reduced ppp also improves the accuracy in determining the axial coordinate (z) of the particle position. It is possible to obtain a theoretical estimate of z by fitting a polynomial as a function of (x, y, Vx, Vy). In all cases, both the transversal components of the position (x, y) and those of the velocity (Vx, Vy) have been measured with good accuracy as shown by the comparison with the numerical simulation. Then, we calculated the difference between the theoretical and the measured z and compared it with R_z (Eq. 17). We have found that the percentage of particles whose position in z is determined with a precision below the expected R_z is 58% for the case with reduced ppp, and 44% for the case with higher ppp.

These data are validated by the exceptional agreement with the numerical simulation as it is shown in Figs. 11 and 12. In Fig. 11 we show the experimental Vz (case B) measured with the original (top row) and the reduced ppp (middle row). We can compare both with the numerical simulation (bottom row). The improvement when the ppp is reduced is evident also in the 3D velocity fields. Figs. 12a and b show the experimental velocity fields and the numerical simulation respectively.

In order to verify that the particles are located accurately the measured data have been interpolated to a rectangular mesh and compared with the iso-surfaces obtained from the numerical simulation (Fig. 12c). The plotted iso-surfaces corresponds to the following velocity values: Vx(m/s)= -0,5, 0, 0.5; Vy(m/s)= -0,2, 0, 0.5; Vx(m/s)= -0,4, 0.4.

6. Conclusions

In this work, 3D velocity fields have been measured in a volume of fluid with a field of view twice the area allowed by the camera sensor, with a magnification M=1, with a very large dimension along the optical axis. Experiments have been carried out with two different particle concentrations.

We have identified the parameters that most influence the Signal to Noise Ratio: noise from the twin image, aliasing and particle concentration. The frequency filter in sideband holography removes the first two, increasing the SNR in such a way that makes it possible to measure in such a large volume.

Particle concentration is the remaining source of noise. Particles near the camera sensor block the further ones reducing significantly the SNR and affecting the velocity measurement in regions far from the camera sensor. An analytical expression has been obtained that directly relates the intensity recorded by the camera sensor with the density of the particles, the size of the recorded volume and the axial position of the particles. In addition, the SNR can be useful for obtaining particle concentration information as it allows particles per pixel (ppp) to be calculated.

A fully automatic algorithm allows us to determine the position of the particles with accuracy lower than the spatial resolution predicted
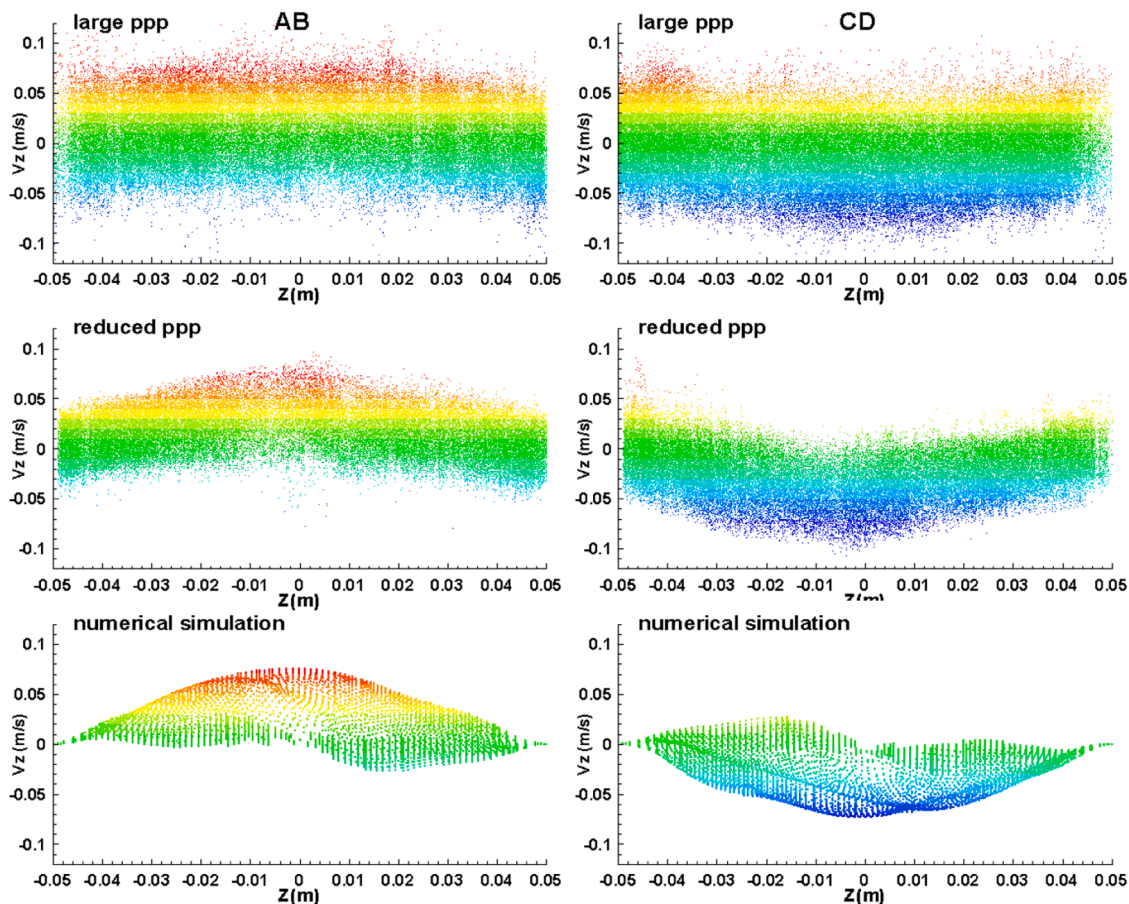

Fig. 11. Case B. Comparison between the numerically simulated Vz (bottom) and the measured Vz in sections AB (left) and CD (right) with large (top) and reduced ppp (middle).
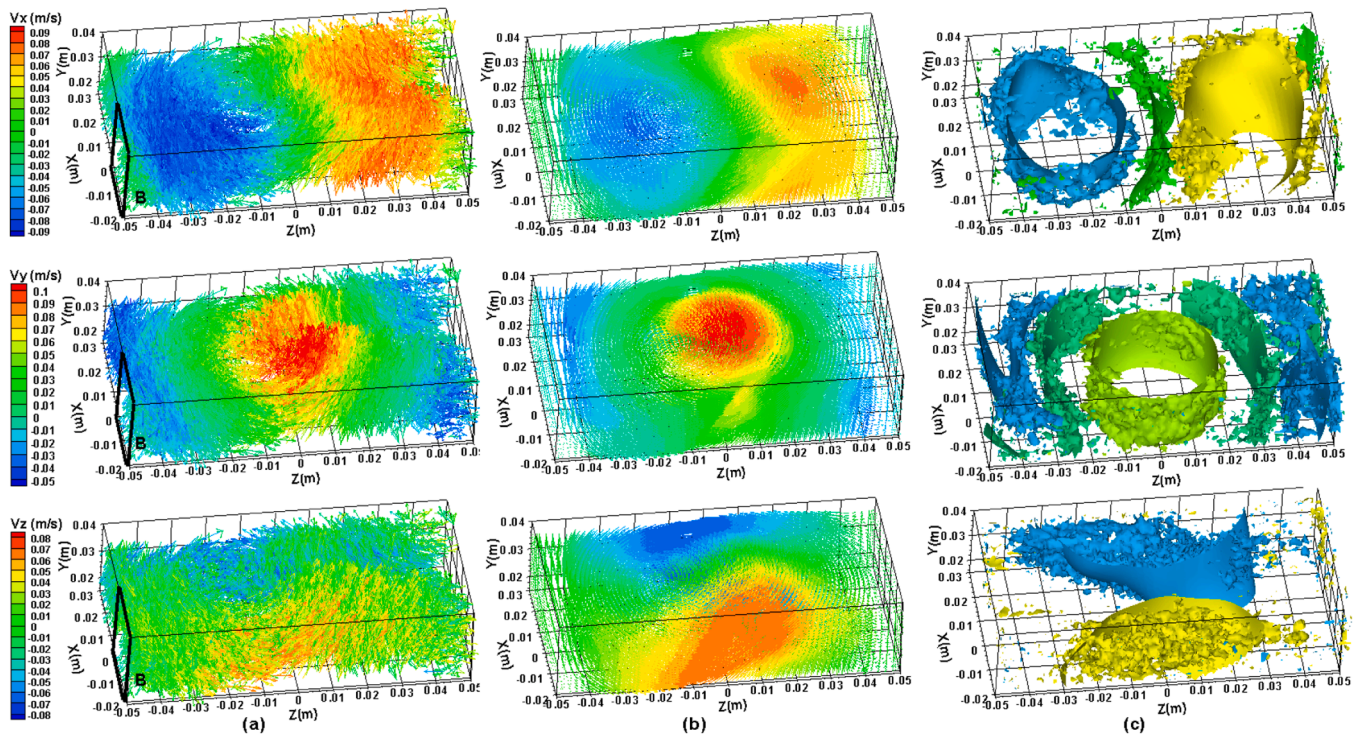
Fig. 12. a) Velocity vector maps obtained for case B with a reduced ppp; b) numerical simulation; c) comparison of the isosurfaces obtained with numerical simulation (smooth isosurfaces) and the experiments.

by theoretical calculation. Its strength lies in the identification of the pixels that most contribute to the particle image. The hologram analysis method has been improved in such a way that fluid volumes can be analyzed, independently of their axial dimension, by dividing them in appropriated sections. Besides, particles are discriminated from their axial position instead of their intensity. We have found that the algorithm performance is not affected by the frequency filter characteristic of the sideband configuration.

Velocity fields have been obtained with a multi-pass, adaptive interrogation process called Adaptive Cross-Correlation Tracking From Beginning. In this method, small 3DIWs can be kept, as if the cross-correlation was performed between consecutive holograms, but avoiding the accumulative error that appears when consecutive recordings are used to follow a particle.

This technique has been validated by measuring the three velocity components in a large volume with a very high ppp (0.23) focusing in different planes in the volume. Once the SNR has been further optimized, by reducing the ppp to 0.06, we have obtained velocity fields remarkably similar to the numerical simulation even for the component parallel to the optical axis.

CRediT authorship contribution statement

Ana Mª López Torres: Investigation, Software, Formal analysis, Validation, Writing – review & editing. **Julia Lobera Salazar:** Software, Formal analysis, Writing – review & editing, Funding acquisition, Project administration. **Nieves Andrés Gimeno:** Conceptualization, Methodology, Writing – original draft. **Adrián Subías Martín:** Investigation. **Eva Mª Roche Seruendo:** Investigation. **Francisco José Torcal Milla:** Writing – review & editing. **Mª Pilar Arroyo de Grandes:** Supervision, Project administration. **Jordi Pallarés Curto:** Software, Formal analysis. **Virginia Palero Díaz:** Conceptualization, Writing – original draft, Writing – review & editing, Validation, Visualization, Funding acquisition.

Declaration of Competing Interest

The authors declare that they have no known competing financial interests or personal relationships that could have appeared to influence the work reported in this paper.

Data availability

Data will be made available on request.

References

[1] Schnars U., Jüptner W.P.O. Digital holography. Springer, Berlin.

[2] Arroyo M.P., Hinsch K.D., Recent developments of PIV towards 3D measurements. editor A Schroder, C.E. Willert, Springer, New York, 2008, p. 127.

[3] Katz J, Sheng J. Applications of holography in fluid mechanics and particle dynamics. Annu Rev Fluid Mech 2010;42:531.

[4] Pu SL, Allano D, Patte-Rouland B, Malek M, Lebrun D, Cen KF. Particle field characterization by digital in-line holography: 3D location and sizing. Exp Fluids 2005;39:1–9.

[5] Palero V, Arroyo MP, Soria J. Digital holography for micro-droplet diagnostics. Exp Fluids 2007;43:185–95.

[6] Palero V, Lobera J, Arroyo MP. Three-component velocity field measurement in confined liquid flows with high speed digital image plane holography. Exp Fluids 2010;49:471–83.

[7] Palero V, Lobera J, Brunet P, Andrés N, Arroyo MP. 3D characterization of the inner flow in an oscillating drop. Exp Fluids 2013;54:1568. https://doi.org/10.1007/s00348-013-1568-5.

[8] Tian L, Loomis N, Domínguez-Caballero JA, Barbastathis G. Quantitative measurement of size and three-dimensional position of fast-moving bubbles in air-water mixture flows using digital holography. Appl Opt 2010;49:1549–54.

[9] Talapatra S, Sullivan J, Katz J, Twardowski M, Czerski H, Donaghay P, Hong J, Jan R, McFarland M, Nayak A, Zhang C. Application of in-situ digital holography in the study of particles, organisms and bubbles within their natural environment. In: Ocean Sensing and Monitoring IV. 8372. International Society for Optics and Photonics; 2012, 837205.

[10] Memmolo P, Miccio L, Paturzo M, Di Caprio G, Coppola G, Netti PA, Ferraro P. Recent advances in holographic 3D particle tracking. Adv Opt Photon 2015;7:713.

[11] Li C, Miller J, Wang J, Koley SS, Katz J. Size distribution and dispersion of droplets generated by impingement of breaking waves on oil slicks. J Geophys Res Ocean 2017;122(10):7938–57.

[12] Hesseling C, Peinke J, Gülker G. Adaptation of reference volumes for correlation based digital holographic particle tracking. Meas Sci Technol 2018;29:45207.

[13] Denis L, Fournier C, Fournel T, Ducottet C. Numerical suppression of the twin image in in-line holography of a volume of micro-objects. Meas Sci Technol 2008; 19:074004.

[14] Ooms T, Koek W, Westerweel J. Digital holographic particle image velocimetry: eliminating a sign-ambiguity error and a bias error from the measured particle field displacement. Meas Sci Technol 2008;19:074003.

[15] Lobera J, Palero V, Roche EM, Gómez-Climente M, López-Torres AM, Andrés N, Arroyo MP. Tilted illumination in-line holographic velocimetry: improvements in the axial spatial resolution. Opt Lasers Eng 2020;134:106280.

[16] Latychevskaia T, Fink HW. Holographic time-resolved particle tracking by means of three-dimensional volumetric deconvolution. Opt. Express 2014;22: 20994–1003.

[17] Lebon B, Perret G, Coëtmellec S, Godard G, Gréhan G, Lebrun D, Brossard J. A digital holography set-up for 3D vortex flow dynamics. Exp Fluids 2016;57:103. https://doi.org/10.1007/s00348-016-2187-8.

[18] Chen Y, Guildenbecher DR, Hoffmeister KNG, Cooper MA, Stauffacher HL, Oliver MS, Washburn EB. Study of aluminum particle combustion in solid propellant plumes using digital in-line holography and imaging pyrometry. Combust Flame 2017;182:225–37.

[19] Toloui M, Mallery K, Hong J. Improvements on digital in-line holographic PTV for 3D wall-bounded turbulent flow measurements. Meas Sci Technol 2017;28: 044009. https://doi.org/10.1088/1361-6501/aa5c4d. 15pp.

[20] López AM, Lobera J, Andrés N, Arroyo MP, Palero V, Sancho I, Vernet A, Pallarés J. Advances in interferometric techniques for the analysis of the three-dimensional flow in a lid-driven cylindrical cavity. Exp Fluids 2020;61:10.

[21] Gómez-Climente M, Lobera J, Arroyo MP, Palero V. Three-dimensional particle size and position measurement by linear complex amplitude Wiener filtering. Opt Express 2022;30(9):15008–23. Apr 25.

[22] Bryngdahl O, Lohmann A. Single-sideband holography. J Opt Soc Am 1968;58: 620–4.

[23] Palero V, Lobera J, Andrés N, Arroyo MP. Shifted knife-edge aperture digital in-line holography for fluid velocimetry. Opt Lett 2014;39:3356–9.

[24] Ramírez C, Lizana A, Iemmi C, Campos J. Inline digital holographic movie based on a double-sideband filter. Opt Lett 2015;40:4142–5.

[25] Goodman JW. Introduction to Fourier optics. New York: MacGraw-Hill International Editions; 1996.

[26] Born M, Wolf E. Principles of optics: electromagnetic theory of propagation, interference and diffraction of light. Cambridge University Press; 1999.

[27] Coupland JM, Lobera J. Holography, tomography and 3D microscopy as linear filtering operations. Meas Sci Technol 2008;19:074012.

[28] Lobera J, Coupland JM. Contrast enhancing techniques in digital holographic microscopy. Meas Sci Technol 2008;19:025501.

[29] Zhang Y, Shen G, Schröder A, Kompenhans J. Influence of some recording parameters on digital holographic particle image velocimetry. Opt Eng 2006;45(7). 075801-075801.

[30] Hesseling C, Homeyer T, Peinke J, Gülker G. Effects of particle locations on reconstructed particle images in digital holography. Appl Opt 2016;55(33): 9532–45.

[31] Royer H. An application of high-speed microholography: the metrology of fogs. Nouv Rev Opt 1974;5:87–9.

[32] Meng H, Anderson WL, Hussain F, Liu DD. Intrinsic speckle noise in in-line particle holography. J Opt Soc Am A 1993;10:2046–58.

[33] Malek M, Allano D, Coëtmellec S, Lebrun D. Digital in-line holography: influence of the shadow density on particle field extraction. Opt Express 2004;12:2270–9.

[34] Wormald SA, Coupland JM. Particle image identification and correlation analysis in microscopic holographic particle image velocimetry. Appl Opt 2009;48:6400–7.

[35] Coupland JM, Lobera-Salazar J, Halliwell NA. Fundamental limitations to the spatial resolution and flow volume that can be mapped using holographic particle image velocimetry. In: Proc. SPIE 4076. Optical Diagnostics for Industrial Applications; 2000. https://doi.org/10.1117/12.397966.

[36] Sancho I, Varela S, Vernet A, Pallares J. Characterization of the reacting laminar flow in a cylindrical cavity with a rotating endwall using numerical simulations and a combined PIV/PLIF technique. Int J Heat Mass Transf 2016;93:155–66.